A Photovoltaics-aided Interlaced Extended Kalman Filter for Distribution Systems State Estimation

Grazia Barchi[a], David Macii[1b]

[a]EURAC Research – Institute for Renewable Energy
via Alessandro Volta, 13/A – 39100, Bozen-Bolzano, Italy
E-mail: grazia.barchi@eurac.edu

[b]University of Trento – Dep. of Industrial Engineering,
Via Sommarive, 9 – 38123, Trento, Italy
E-mail: david.macii@unitn.it

Abstract

Distribution system state estimation (DSSE) is essential for smart grid monitoring and control. Bus voltage phasors and, consequently, DSSE uncertainty can be significantly affected by photovoltaic (PV) penetration, even when suitable hosting capacity strategies are adopted to keep voltage levels within given limits. In this paper, it is shown that the state estimation uncertainty achievable with algorithms exploiting PV information can be significantly lower than using classic techniques, such as the Weighted Least Squares approach that is still widely adopted at the distribution level. The proposed analysis relies on an Interlaced Extended Kalman Filter (IEKF) that, in the prediction step, relies on the available information on active and reactive power injections. The use of an interlaced implementation makes the estimator more robust to zero-power injections, which otherwise could make the Kalman innovation matrix ill-conditioned. In the update step, the PV power data measured on the field, possibly supported by Phasor Measurement Units (PMUs), complement the traditional virtual and pseudo-measurements, or the aggregated smart meter data. The results of one-year-long simulations confirm the benefits of including the available information on PV generation on state estimation uncertainty.

Keywords: Distribution systems, state estimation, photovoltaic power system, power system measurements, uncertainty.

1. Introduction

The penetration of renewable-based distributed energy resources is both one of the main opportunities for smart grid evolution and one of the main challenges for its stable operation. Limiting the attention to the Photovoltaics (PV) case, new generators with a total capacity of about 99 GW were connected to the grid in 2017, with a year-on-year increase of almost 30% compared to 2016 [1].

In general, solar generation affects not only the inherent variability of RMS voltage amplitude and phase (regarded as system state variables) at different buses, but also the performance and stability of the algorithms used to estimate these quantities in real-time. As known, PV penetration may lead to violations of the voltage limits established by national or international regulations due to reverse power flows. The American National Standards Institute (ANSI) Standard C84.1-2016 specifies indeed that the voltage magnitude of residential loads has to lie within ±5% of the nominal value [2]. According to the European Standard (EN) 50160:2010 instead, Medium- and Low-voltage levels should not exceed ±10% of the declared value for 95% of week under normal operating conditions [3]. Besides voltage rises, a large PV penetration may have several other critical consequences on distribution networks, such as voltage fluctuations due to solar power intermittency, voltage and current imbalances, harmonic distortion (mainly caused by

PV inverters) and possible safety hazards due to unintentional islanding [4]. Of course, maximizing the *hosting capacity* (i.e. the amount of PV-based distributed generation for which given operational constraints on a feeder are not violated) is of paramount importance for renewable-based smart grid evolution [5, 6]. Even if a variety of measures (e.g., adjustable switched capacitor banks, on-load tap changers, network topology reconfiguration and above all, VAR-capable PV inverters) exist to mitigate voltage fluctuations and overvoltages, the impact of solar penetration on Distribution System State Estimation (DSSE) could be potentially critical and it has not been deeply investigated yet. In fact, even when the system voltage is kept under control, the combination of: solar generation intrinsic variability, limited system observability and heterogeneous measurement uncertainty contributions may significantly affect state estimation behavior. At the distribution level, this problem is even more critical not only because the number of measurement points and deployed instruments is usually smaller than in transmission systems, but also because the radial structure and the higher R/X ratio of typical distribution systems make them more sensitive to the penetration of distributed energy resources [7, 8]. In this respect, one of the open research challenges of DSSE is the definition and inclusion of models able to exploit (or at least mitigate the impact of) generation variability on state estimation algorithms [9], like in the case of large

PV penetration [10, 11]. This paper provides a possible solution to this problem, by proposing a PV-aided Interlaced Extended Kalman Filter (PV-IEKF) conceived to be numerically robust to zero power injections and able to exploit the available information on solar generation. The key advantage of the proposed approach is that it improves DSSE accuracy and robustness with no need to revolutionize the overall measurement infrastructure. In the rest of this manuscript, the novelty and the benefits of the proposed estimator are highlighted in Section 2 in the context of some related work. Section 3 deals with both models description and PV-IEKF implementation. Section 4 presents two case studies and analyzes the intrinsic variability of state variables due to growing PV penetration and seasonal fluctuations. Finally, in Section 5 the state estimation results obtained with the PV-IEKF using two different measurement setups are reported and compared with those obtained by using a classic state-of-the-art DSSE algorithm.

2. Related Work

In general, the purpose of state estimation algorithms for transmission or distribution systems is to determine the node voltage or branch current phasors at a given time by using only a limited amount of available information, that can be obtained from historical data records (pseudo-measurements), or can be collected through Supervisory Control And Data Acquisition (SCADA) systems, intelligent electronics devices or, more recently, from Phasor Measurement Units (PMUs) [12, 13]. In general, the state estimation algorithms can be classified as static or dynamic [14]. The static estimators rely solely on the data measured at a given time. Thus, no system dynamics is included in the model. The most popular static state estimator (which is used for both transmission and distribution systems) is based on the Weighted Least Squares (WLS) method [15], possibly enhanced through adaptive, data-driven preprocessing [16]. Alternative static estimators conceived to be robust to non-Gaussian measurement errors have been recently proposed as well [17].

Conversely, the dynamic state estimators rely on a system model describing state evolution and an output model that can be used to observe the state variables. The dynamic estimators estimate the state recursively by applying a prediction step and an update step. Depending on i) how the underlying system model is defined and ii) the level of severity of possible nonlinearities affecting either the system or the measurement model, many different kinds of dynamic state estimators have been proposed for power systems, e.g., fully linear standard Kalman Filters (KFs) [18], Extended Kalman Filters (EKFs) in the case of moderate nonlinearities [19, 20], or robust Unscented Kalman filters (UKF) when the effect of nonlinearity errors may jeopardize estimation results [21]. In some cases, hierarchical Kalman-based solutions are used first to partition and then to combine the estimates of the state variables related to different areas of large-scale power systems, in order to reduce the computational burden [22]. According to the recent analysis reported in [23], the dynamic state estimators can be roughly classified either as Forecasting-aided State Estimation

(FASE) or Tracking State Estimators (TSE). Both categories usually rely on a linearized system model and on a nonlinear measurement model. However, in the former case, the state transition matrix is computed from the time series of the recent state variables, usually by using an exponentially decreasing set of weights (Holt-Wilters approach). Additionally, a trend input vector is included to track smooth (i.e. almost linear) variations.

In TSEs instead, the state transition matrix is just the identity matrix and the system state variability is caused by an input random noise [24]. Rigorously speaking, it is highlighted in [23] that both categories suffer from serious drawbacks in the presence of an increasing penetration of distributed and flexible loads. This is due to: i) the underlying models that are too simple to describe sharp operating conditions changes and ii) the diagonal structure of the state transition matrix that totally disregards the correlation between state variables [25]. Moreover, even if the FASE solutions perform generally better than the TSE ones at the transmission level, they can be hardly applied to distribution systems, because the forecasting algorithm used to build the transition matrix requires the time series of the state variable values at all buses. However, in most distribution systems such data are not available due to the scarcity of measurement points, which also greatly limits overall system observability [26]. Therefore, considering the existing infrastructural constraints, a TSE approach is not only easier to apply, but also less sensitive to large potential modeling errors, which could be further stressed by the strongly time-varying nature of renewable-based generated power profiles. This is why the solution proposed in this paper relies instead on a TSE approach. However, unlike the classic TSE estimator [24], the idea of this work is to include in the dynamic estimator the available information about PV generation both in the prediction step (considering the average daily variations of PV power profiles estimated in different months) and in the update step (by using the values of PV generated power collected in real-time from the meters located at the generation sites). Such additional information can effectively complement: the typical pseudo-measurements obtained from the aggregation of historical load data collected from existing (legacy) meters, the load data that are collected in real-time (and with a much lower uncertainty) by an increasing share of new-generation smart meters and the voltage phasors measured directly by a set of PMUs, if available [27].

To the best of Authors' knowledge, not many research works are explicitly focused on the use of distributed generation data for DSSE. A study on the impact of PV penetration on low-voltage WLS-based DSSE is presented in [11]. That approach relies on a Gaussian mixture model to generate load pseudo-measurements. However, the PV-IEKF approach described in this paper proves to perform better than the WLS in the same conditions, as it will be shown in Section 5. In [28], the Authors propose a hybrid technique based on the WLS method and the firefly algorithm to reach a reliable and accurate state estimation of grids where renewable energy sources are employed. However, the reported results are quite a few and the impact of time-varying power profiles is unclear. Finally, in [29], a DSSE algorithm based on the combination of Nelder-Mead simplex

and Particle Swarm Optimization is used to determine loads and generators power. However, this approach can be hardly compared with other solutions published in the literature, as the state variables are not the bus voltage or the line current phasors, as customary in DSSE problems, but rather the power values themselves. In addition, the performance analysis does not take into account the power fluctuations due to time-varying load or generation operating conditions, as instead presented in this work.

A further novel contribution of the proposed PV-IEKF estimator is the interlaced filter implementation that ensures a higher numerical robustness than a standard one, as proved in Appendix B. The rationale underlying this approach stems from the potential huge differences between the variances of the power injections at buses affected by significant load fluctuations and/or PV penetration and the negligible variances at buses with zero power injections.

As a last remark, the effect of PMUs on PV-IEKF estimation performance is investigated in the last part of the paper since such instruments are currently regarded as the most effective ones to support state estimation in distribution systems, as shown for instance in [12, 18, 30, 31]. Therefore, even if they are not strictly needed for PV-IEKF implementation, analyzing their impact on state estimation accuracy is a topical issue.

3. Models and State Estimator Description

The state of a distribution systems is usually expressed in terms of either bus voltage or line current phasors expressed either in polar or in rectangular coordinates [32]. In the following, without loss of generality, the state of the system will be expressed in terms of bus voltage amplitude and phase.

3.1. System and measurement models

Let the bold symbols represent vectorial quantities. Given a distribution system consisting of N buses, its state is expressed by $\mathbf{x} = [\theta^1, ..., \theta^N, V^1, ..., V^N]^T$, where the variables θ^i and V^i are the phase and the Root Mean Square (RMS) amplitude, respectively, of the voltage phasor at the ith bus (for $i = 1, \ldots, N$). In the following, the slack bus will be conventionally labeled as bus 1. Usually, θ^1 can be excluded from $\mathbf{x}$, as it is conventionally set to 0, unless it is measured directly by a PMU. From power systems theory, it is well known that the active and reactive power injections at the ith bus are related to the chosen state variables by the following nonlinear expressions, i.e. [15]

$$P^i = P_G^i - P_L^i = V^i \sum_{j=1}^N V^j [\Re\{Y^{ij}\}\cos\theta^{ij} + \Im\{Y^{ij}\}\sin\theta^{ij}]$$

$$Q^i = Q_G^i - Q_L^i = V^i \sum_{j=1}^N V^j [\Re\{Y^{ij}\}\sin\theta^{ij} - \Im\{Y^{ij}\}\cos\theta^{ij}]$$
(1)

where $\Re\{Y^{ij}\}$ and $\Im\{Y^{ij}\}$ are the real and imaginary parts of the element (i, j) of the network admittance matrix and $\theta^{ij} = \theta^i - \theta^j$. Finally, P_G^i, Q_G^i and P_L^i, Q_L^i, are the active and reactive power

generated by the distributed PV units or absorbed by loads, respectively, at the ith bus. Such quantities as well as the state variables change over time. However, in (1) the time variable is omitted for the sake of brevity.

Let $\mathbf{u}_G = [P_G^2, ..., P_G^N, Q_G^2, ..., Q_G^N]^T$ and $\mathbf{u}_L = [P_L^2, ..., P_L^N, Q_L^2, ..., Q_L^N]^T$ be the vectors comprising the active/reactive generation and load power profiles at buses different from the slack bus. If the expressions in (1) are rearranged in a matrix form for $i = 2, \ldots, N$ (i.e. excluding the slack bus power injections that generally are linearly dependent on the others), after linearizing and discretizing the resulting system of equations between instants t_{k-1} and t_k (with k denoting the kth sampling period, e.g. in the order of a few minutes), an additional linearly independent equation for bus 1 is needed to make the linearized system matrix square and invertible. In practice, the relationship between the slack bus voltage V^1 and the system nominal voltage $\bar{V}$ can be used to this purpose assuming, without loss of generality, that $\theta^1 = 0$ [33]. As a consequence, after a few algebraic steps reported in Appendix A, the resulting discrete-time system is given by

$$\mathbf{x}_k = \mathbf{x}_{k-1} + G_{k-1}(\Delta\mathbf{u}_{G_k} - \Delta\mathbf{u}_{L_k}) + \nu_k$$
(2)

where input vectors $\Delta\mathbf{u}_{G_k}$ and $\Delta\mathbf{u}_{L_k}$ include the variations of active and reactive generated and absorbed power between t_{k-1} and t_k, while $G_{k-1} = -A_{k-1}^{-1} B_{k-1}$ is the input matrix depending on the system Jacobian matrices A_{k-1} (with respect to state variables) and B_{k-1} (with respect to input variables), respectively (see expressions (A.4) and (A.5) in Appendix A for details). Finally, $\nu_k = -A_{k-1}^{-1} \mathbf{e}_k$ can be regarded as the process noise due to the linearization errors in $\mathbf{e}_k$. It is worth emphasizing that, even if the adopted model is similar to the model proposed in [24], in this case the power injected by possible PV units is part of the inputs to the system and it will be used in the prediction step of the proposed TSE, as it will be explained in Section 3.2. Of course, if no PV generator is connected to a given bus, the corresponding entry of vector $\Delta\mathbf{u}_{G_k}$ will be 0. Moreover, unlike the models described in [24] and [33], in this paper the load or PV active/reactive power profiles (as well as the related variations) are not assumed to be purely white random sequences, but are more realistically modeled by the superimposition of a deterministic term (modeling daily and monthly trends) and a zero-mean random process modeling the short-term and weakly correlated residual fluctuations, i.e.

$$\Delta\mathbf{u}_{G_k} = \mathbf{d}_{G_k}^m + \boldsymbol{\epsilon}_{G_k}^m \quad \text{and} \quad \Delta\mathbf{u}_{L_k} = \mathbf{d}_{L_k}^m + \boldsymbol{\epsilon}_{L_k}^m$$
(3)

where $\mathbf{d}_{G_k}^m$ and $\mathbf{d}_{L_k}^m$, for $m = \{$Jan., $\ldots$, Dec.$\}$, represent the variations of active and reactive power injected by the PV units or absorbed by loads between t_{k-1} and t_k within the same month, while $\boldsymbol{\epsilon}_{G_k}^m$ and $\boldsymbol{\epsilon}_{L_k}^m$ are the respective random fluctuations. This model makes the EKF estimator formally more correct than in [24] and [33], since most of the correlation in time between input data is "captured" by $\mathbf{d}_{G_k}^m$ and $\mathbf{d}_{L_k}^m$, thus not affecting the covariance of $\boldsymbol{\epsilon}_{G_k}^m$ and $\boldsymbol{\epsilon}_{L_k}^m$. In practice, $\mathbf{d}_{G_k}^m$ and $\mathbf{d}_{L_k}^m$ can be obtained in a variety of ways, e.g., through direct measurements (if available) or through suitable forecasting algorithms. For

instance, for PV generation, a clear-sky model or a persistence-based predictor could be used. However, as explained in Section 5, a different and quite simple approach is used in this paper to ensure that the random fluctuations exhibit a zero mean, which is essential for a correct Kalman filter implementation.

Of course, besides the system model, a measurement model is also needed to implement the state estimator. If $\mathbf{z}_k$ denotes the vector of quantities that can be directly observed at a given time t_k, and if $\mathbf{v}_k$ is the vector of the respective measurement uncertainty contributions, the measurement model can be generally expressed as

$$\mathbf{z}_k = \mathbf{h}(\mathbf{x}_k) + \mathbf{v}_k \qquad (4)$$

where each element of vector function $\mathbf{h}(\mathbf{x}_k)$ models the relationship between one of the observed quantities and the state variables at time t_k. In practice, various kinds of measurements can be included in (4), e.g. active and reactive power measurements or synchrophasor measurements. In this paper, without loss of generality, two different measurement setups will be adopted to evaluate state estimation performance, as explained in Section 5.1.

3.2. PV-aided Interlaced Extended Kalman Filter

By combining (2) with (3), the system model to be used for EKF implementation becomes

$$\mathbf{x}_k = \mathbf{x}_{k-1} + G_{k-1}(\mathbf{d}_{G_k}^m - \mathbf{d}_{L_k}^m) + \mathbf{w}_k^m \quad m = \{\text{Jan.}, \ldots, \text{Dec.}\} \quad (5)$$

where $\mathbf{w}_k = G_{k-1}(\boldsymbol{\epsilon}_{G_k}^m - \boldsymbol{\epsilon}_{L_k}^m) + \boldsymbol{\nu}_k$ can be regarded as the cumulative process noise. Note that the elements of $\mathbf{w}_k$ result from the linear combination of several zero-mean random independent contributions, that are also weakly correlated in time. Therefore, each element of the noise vector tends to be white and normally distributed because of the Central Limit Theorem under the so-called Lindeberg's condition. Although (4) and (5) in principle can be directly used for EKF implementation, a classic EKF hides the risk of numerical instability if zero-injection virtual measurements are used in (4) [34]. This is due to the fact that, in the case of zero-power injections, the ratio between the maximum and the minimum eigenvalues of the so-called innovation covariance matrix could be very large (ideally infinite), thus making the Kalman gain matrix ill-conditioned. This problem could be particularly critical in the case of significant PV penetration because the covariance matrix of the PV power fluctuations is added to the covariance matrix of load variations (as it will be shown in the following), thus potentially increasing the maximum eigenvalues of the prediction covariance matrix, and consequently of the whole innovation matrix.

To address this issue, an interlaced Kalman filter implementation is adopted in this paper. The idea of this approach is to partition a system into multiple smaller subsystems, whose individual states are estimated by distinct, although interacting, EKFs [35]. In the proposed PV-IEKF, state and measurement vectors as well as the related models are rearranged and split into two parts: one related to slack bus and zero-injection buses only, and the other including all the other buses. To define
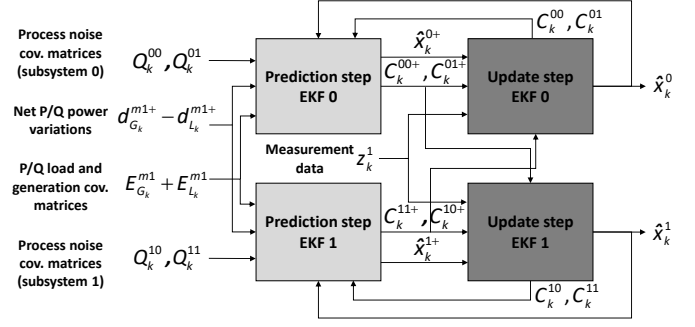

Figure 1: Block diagram of the proposed PV-IEKF for distribution system state estimation.

the state estimator structure (whose block diagram is shown in Fig. 1), let us rearrange (5) and (4), respectively as

$$\begin{bmatrix} \mathbf{x}_k^0 \\ \mathbf{x}_k^1 \end{bmatrix} = \begin{bmatrix} \mathbf{x}_{k-1}^0 \\ \mathbf{x}_{k-1}^1 \end{bmatrix} + \begin{bmatrix} G_{k-1}^{00} & G_{k-1}^{01} \\ G_{k-1}^{10} & G_{k-1}^{11} \end{bmatrix} \begin{bmatrix} \mathbf{0} \\ \mathbf{d}_{G_k}^{m1} - \mathbf{d}_{L_k}^{m1} \end{bmatrix} + \begin{bmatrix} \mathbf{w}_k^{m0} \\ \mathbf{w}_k^{m1} \end{bmatrix}$$
$$\begin{bmatrix} \mathbf{z}_k^0 \\ \mathbf{z}_k^1 \end{bmatrix} = \begin{bmatrix} \mathbf{h}^0(\mathbf{x}_k^0, \mathbf{x}_k^1) \\ \mathbf{h}^1(\mathbf{x}_k^0, \mathbf{x}_k^1) \end{bmatrix} + \begin{bmatrix} \mathbf{v}_k^0 \\ \mathbf{v}_k^1 \end{bmatrix} \qquad (6)$$

where superscript 0 refers to the subsystem of slack and zero-injection buses, while superscript 1 refers to the subsystem comprising all the other buses.

3.2.1. Prediction step

if $\hat{\mathbf{x}}_{k-1}^0$ and $\hat{\mathbf{x}}_{k-1}^1$ denote the state of subsystems 0 and 1 estimated at time t_{k-1}, it results from (6) that the respective predicted states are given by [36]

$$\hat{\mathbf{x}}_k^{0+} = \hat{\mathbf{x}}_{k-1}^0 + G_{k-1}^{01}(\mathbf{d}_{G_k}^{m1} - \mathbf{d}_{L_k}^{m1})$$
$$\hat{\mathbf{x}}_k^{1+} = \hat{\mathbf{x}}_{k-1}^1 + G_{k-1}^{11}(\mathbf{d}_{G_k}^{m1} - \mathbf{d}_{L_k}^{m1}). \qquad (7)$$

Similarly, if C_{k-1}^{00}, C_{k-1}^{11}, C_k^{00+} and C_k^{11+} denote the covariance matrices of the respective estimated and predicted state vectors, then it easily follows from (6) that

$$C_k^{00+} = C_{k-1}^{00} + W_k^{00} = C_{k-1}^{00} + G_{k-1}^{01}(E_{G_k}^{m1} + E_{L_k}^{m1})G_{k-1}^{01^T} + Q_k^{00}$$
$$C_k^{11+} = C_{k-1}^{11} + W_k^{11} = C_{k-1}^{11} + G_{k-1}^{11}(E_{G_k}^{m1} + E_{L_k}^{m1})G_{k-1}^{11^T} + Q_k^{11}. \qquad (8)$$

where W_k^{00}, W_k^{11}, Q_k^{00} and Q_k^{11} are the diagonal blocks of the covariance matrices of noise vectors $\mathbf{w}_k$ and $\boldsymbol{\nu}_k$, respectively, while $E_{G_k}^{m1}$ and $E_{L_k}^{m1}$ are the covariance matrices of the elements of $\boldsymbol{\epsilon}_{G_k}^m$ and $\boldsymbol{\epsilon}_{L_k}^m$ after excluding the zero-injection buses. It is important to highlight that even though C_k^{00+} and C_k^{11+} do not depend on the cross-covariance of the subsystem states estimated at time t_{k-1}, $\hat{\mathbf{x}}_k^{0+}$ and $\hat{\mathbf{x}}_k^{1+}$ can be correlated. In fact, matrices

$$C_k^{01+} = C_{k-1}^{01} + W_k^{01} = C_{k-1}^{01} + G_{k-1}^{01}(E_{L_k}^{m1} + E_{G_k}^{m1})G_{k-1}^{11^T} + Q_k^{01},$$
$$C_k^{10+} = C_k^{01+^T} \qquad (9)$$

are not null. Therefore, such terms cannot be neglected and have to be taken into account in the update step of the filter.

3.2.2. Update step

Based on classic Kalman filter theory, the estimates of the subsystems state at time t_k are given by

$$
\begin{aligned}
\hat{\mathbf{x}}_k^0 &= \hat{\mathbf{x}}_k^{0+} + K_k^{01}[\mathbf{z}_k^1 - \mathbf{h}^1(\hat{\mathbf{x}}_k^{0+}, \hat{\mathbf{x}}_k^{1+})] + K_k^{00}[\mathbf{z}_k^0 - \mathbf{h}^0(\hat{\mathbf{x}}_k^{0+}, \hat{\mathbf{x}}_k^{1+})] \\
\hat{\mathbf{x}}_k^1 &= \hat{\mathbf{x}}_k^{1+} + K_k^{11}[\mathbf{z}_k^1 - \mathbf{h}^1(\hat{\mathbf{x}}_k^{0+}, \hat{\mathbf{x}}_k^{1+})] + K_k^{10}[\mathbf{z}_k^0 - \mathbf{h}^0(\hat{\mathbf{x}}_k^{0+}, \hat{\mathbf{x}}_k^{1+})]
\end{aligned}
\tag{10}
$$

where $\mathbf{z}_k^1$ is the vector of the measurement data available at time t_k, $\mathbf{z}_k^0$ is the vector of virtual measurements at zero-injection buses (plus the voltage measurement at the slack bus), while K_k^{00}, K_k^{01}, K_k^{11}, and K_k^{10} result from the block partition of the overall Kalman gain, i.e.

$$
K_k = \begin{bmatrix} K_k^{00} & K_k^{01} \\ K_k^{10} & K_k^{11} \end{bmatrix} = \begin{bmatrix} C_k^{00+} & C_k^{01+} \\ C_k^{01+^T} & C_k^{11+} \end{bmatrix} \begin{bmatrix} H_k^{00^T} & H_k^{10^T} \\ H_k^{01^T} & H_k^{11^T} \end{bmatrix} \begin{bmatrix} L_k^{00} & L_k^{01} \\ L_k^{01^T} & L_k^{11} \end{bmatrix}. \tag{11}
$$

In (11), H_k^{00}, H_k^{01} and H_k^{10}, H_k^{11} are the Jacobian matrices of $\mathbf{h}^0(\mathbf{x}^0, \mathbf{x}^1)$ and $\mathbf{h}^1(\mathbf{x}^0, \mathbf{x}^1)$ with respect to variables $\mathbf{x}^0$ and $\mathbf{x}^1$, respectively, computed at $\hat{\mathbf{x}}_k^{0+}$ and $\hat{\mathbf{x}}_k^{1+}$. Finally, matrices L_k^{00}, L_k^{01} and L_k^{11} result from the blockwise inversion further details are reported in Appendix B) of the innovation covariance matrix of the whole system, i.e.

$$
\begin{bmatrix} L_k^{00} & L_k^{01} \\ L_k^{01^T} & L_k^{11} \end{bmatrix} = \begin{bmatrix} S_k^{00} & S_k^{01} \\ S_k^{01^T} & S_k^{11} \end{bmatrix}^{-1} = \tag{12}
$$

$$
\left(\begin{bmatrix} H_k^{00} & H_k^{01} \\ H_k^{10} & H_k^{11} \end{bmatrix} \begin{bmatrix} C_k^{00+} & C_k^{01+} \\ C_k^{10+} & C_k^{11+} \end{bmatrix} \begin{bmatrix} H_k^{00^T} & H_k^{10^T} \\ H_k^{01^T} & H_k^{11^T} \end{bmatrix} + \begin{bmatrix} R_k^{00} & 0 \\ 0 & R_k^{11} \end{bmatrix} \right)^{-1}
$$

with R_k^{00} and R_k^{11} being the covariance matrices of measurement uncertainty contributions $\mathbf{v}_k^0$ and $\mathbf{v}_k^1$. In Appendix B it is shown that the blockwise matrix inversion of (12) relies on submatrices with a narrower eigenvalue range than the full matrix. Consequently, the subsystems matrix condition numbers are smaller and the risk of numerical instability is lower than using a monolithic EKF. Finally, the covariance matrices associated with $\hat{\mathbf{x}}_k^0$ and $\hat{\mathbf{x}}_k^1$ as well as the cross-covariance between them are given by

$$
\begin{aligned}
C_k^{00} &= C_k^{00+} - \begin{bmatrix} K^{00} & K^{01} \end{bmatrix} \begin{bmatrix} H^{00} \\ H^{10} \end{bmatrix} C^{00+} - \begin{bmatrix} K^{00} & K^{01} \end{bmatrix} \begin{bmatrix} H^{01} \\ H^{11} \end{bmatrix} C^{10+} \\
C_k^{11} &= C_k^{11+} - \begin{bmatrix} K^{10} & K^{11} \end{bmatrix} \begin{bmatrix} H^{01} \\ H^{11} \end{bmatrix} C^{11+} - \begin{bmatrix} K^{10} & K^{11} \end{bmatrix} \begin{bmatrix} H^{00} \\ H^{10} \end{bmatrix} C^{01+} \\
C_k^{01} &= C_k^{01+} - \begin{bmatrix} K^{00} & K^{01} \end{bmatrix} \begin{bmatrix} H^{00} \\ H^{10} \end{bmatrix} C^{01+} - \begin{bmatrix} K^{00} & K^{01} \end{bmatrix} \begin{bmatrix} H^{01} \\ H^{11} \end{bmatrix} C^{11+} \\
C_k^{10} &= C_k^{01^T}
\end{aligned}
\tag{13}
$$

In practice, (13) can be preferably computed through the so-called Joseph form [36]. That alternative formulation, although more computationally intensive, prevents by construction that matrices C_k^{00}, C_k^{01}, C_k^{10} and C_k^{11} are not positive definite simply because of numerical errors, thus reducing the risk of Kalman filter divergence.

4. Case Study Description

Two Medium-Voltage (MV) case studies are considered in the rest of the paper, i.e. a simplified and modified version of the IEEE 37-bus radial feeder[2], and the rural 85-bus distribution system reported in [37]. Such distribution systems were selected among others because they both include a significant fraction (i.e. about 30%) of zero-injection buses. In the following subsections, first, the simulation settings for load and PV generation in both case studies are described. Then, the single-phase equivalent power flow analyses under time-varying conditions of PV generation and load are performed repeatedly to compute the "true" values of the state variables to be estimated in different seasons of the year as well as their intrinsic fluctuations. The respective state estimation results are instead reported in Section 5.

4.1. Settings for Load and PV generation

The reference declared voltage of the 37-bus and the 85-bus distribution systems are $\bar{V} = 4.8$ kV and $\bar{V} = 11$ kV, respectively. The state variables values of the IEEE 37-bus system under nominal conditions (assuming initially 0% PV penetration and a base apparent power of 1 MVA) are reported in Tab. 1 for one phase only, along with the respective nominal active and reactive loads. Observe that the original bus identification labels of the IEEE 37-bus feeder (between brackets in the first column of the Table) are orderly renumbered for the sake of clarity. The state variables values of the IEEE 85-bus system under nominal conditions are not shown for the sake of brevity, but they can be found in [37].

In both cases, load and PV generated power values are assumed to be available every 15 minutes over 1 year of simulation time, since this is the expected reporting period of the next-generation smart meters, which will be used for state estimation [38]. No other distributed generators (except the PV units) are installed in the system. Therefore, when no PV generators are deployed, all the load power is provided by the slack bus. The power flow analysis and, consequently, the actual state of the grid at every time step t_k, for $k = 1, \ldots, 35040$, is computed through the Matpower toolbox [39]. Further details about how load and PV generated power profiles are synthesized in both case studies are reported below.

4.1.1. Load profiles

The load active power fluctuations at all buses other than both the slack bus and the zero-injection buses result from the aggregation of the electricity profiles of residential and office buildings of various size, taking into account daily and seasonal variations due to different heating or cooling needs as well as the actual number of occupants [40]. The profiles of different buildings are synthesized by the Matlab application described in [41] and are aggregated to ensure that the total yearly average loads are approximately equal to the nominal values shown in Tab. 1

---

[2]http://sites.ieee.org/pes-testfeeders/resources/

Table 1: Nominal static voltage amplitude (in p.u.) and phase (in centiradians - crad) as well as active and reactive power values at different buses of the IEEE 37-bus test distribution system. The rightmost column shows the relative standard deviations of the load fluctuations over 1 year.

Bus no.	V^i [p.u.]	θ^i [crad]	P_L^i [kW]	Q_L^i [kvar]	$\sigma_{L_r}^i$ [%]
1 (799)	1.000	0	0	0	0
2 (701)	0.989	-0.158	140	70	32.6
3 (712)	0.978	-0.235	85	40	32.4
4 (713)	0.977	-0.263	85	40	32.7
5 (714)	0.973	-0.277	21	10	59.7
6 (718)	0.972	-0.269	85	40	31.8
7 (720)	0.969	-0.298	85	40	32.6
8 (722)	0.965	-0.253	140	70	32.4
9 (724)	0.965	-0.250	42	21	29.8
10 (725)	0.967	-0.302	42	21	29.7
11 (727)	0.972	-0.303	42	21	29.7
12 (728)	0.971	-0.308	42	21	29.7
13 (729)	0.970	-0.304	42	21	29.7
14 (730)	0.969	-0.314	85	40	30.4
15 (731)	0.966	-0.309	85	40	32.6
16 (732)	0.966	-0.308	42	21	30.7
17 (733)	0.966	-0.310	85	40	31.4
18 (734)	0.965	-0.305	42	21	31.4
19 (735)	0.965	-0.295	85	40	29.9
20 (736)	0.969	-0.301	42	21	39.7
21 (737)	0.963	-0.310	140	70	31.6
22 (738)	0.963	-0.312	126	62	28.9
23 (740)	0.963	-0.309	85	40	32.1
24 (741)	0.965	-0.311	42	21	37.2
25 (742)	0.978	-0.234	85	40	31.0
26 (744)	0.971	-0.310	42	21	36.8
27 (702)	0.980	-0.251	0	0	0
28 (703)	0.974	-0.316	0	0	0
29 (704)	0.974	-0.279	0	0	0
30 (705)	0.979	-0.239	0	0	0
31 (706)	0.968	-0.307	0	0	0
32 (707)	0.965	-0.258	0	0	0
33 (708)	0.967	-0.312	0	0	0
34 (709)	0.968	-0.312	0	0	0
35 (710)	0.965	-0.298	0	0	0
36 (711)	0.964	-0.312	0	0	0
37 (775)	0.968	-0.312	0	0	0

(for the 37-bus system) and in Tab. A.3.2 of [37] (for the 85-bus system), respectively. The maximum standard deviations of the aggregated load profile over 1 year at every bus relative to the respective nominal values are usually below 33%, with a few exceptions. It is worth noticing that the load profiles at different buses can be strongly correlated [42]. In the cases at hand, the correlation coefficients between different buses can be so large as 0.95.

The load reactive power profiles exhibit the same pattern as the active ones, but they are scaled down depending on the power factor at each bus. As a consequence, the correlation coefficients between active and reactive power injection at the same bus is 1.

4.1.2. PV power profiles

The PV power generation profiles are synthesized by following an approach similar to the one described in [43], but they rely on the same set of irradiance data to maintain a certain spatial correlation between different profiles, which is quite reasonable due to the limited area of the distribution systems considered (i.e., a few km^2). In particular, starting from the experimental irradiance data collected in the solar park of the Bolzano-Dolomiti airport (Bolzano, Italy) every 15 minutes in 2017, first the mean value and the standard deviation of the irradiance data at the same time of the day of the same month were computed. Afterwards, such sequence of mean value and standard deviation was used to determine the parameters of different Beta probability density functions (PDFs) modeling solar irradiance, as explained in [43], but with 15-minute rather than hourly resolution. Finally, a sequence of Beta-distributed random variables (one for each bus), with parameters changing as a function of both the time of the day and the month was used to perturb the daily average solar irradiance profile measured in each month of the year. As a result, the PV active power profile generated at the ith bus is given by

$$P_{G_k}^i = r_k^i A_{PV}^i \eta_{PV}^i \eta_c^i [1 + \gamma^i (T_k - T_0)] F_{PV}^i \quad i = 1, ..., N \quad (14)$$

where

- r_k^i is the synthetic solar irradiance profile associated with the i−th bus;

- A_{PV}^i is the total area of the PV modules connected to bus i depending on the chosen PV penetration level. If no PV generator is connected to bus i, then $A_{PV}^i = 0$;

- $\eta_{PV}^i = 16\% \pm 3\%$ is the PV conversion efficiency of the modules linked to bus i, in line with the efficiency values reported in [44];

- $\eta_c^i = 98\%$ is the DC/AC conversion efficiency in accordance with state-of-the art inverter technologies [45];

- $\gamma^i = -0.3 \pm 0.0750$ %/K is the temperature coefficient affecting PV conversion efficiency at bus i when the temperature of PV modules is different from the reference one (i.e., $T_0 = 298$ K).

- T_k is the sequence of temperature values measured every 15 minutes on the PV modules of the Bolzano-Dolomiti airport the solar park throughout year 2017;

- Finally, F_{PV}^i is the operating power factor of the PV units linked to bus i, assuming that the inverter-based PV technology is capable to export or to consume reactive power [43]. Even if a variety of distributed or centralized control strategies exist to determine the active and reactive power set-points of smart PV inverters [46, 47], the solution adopted in this paper is quite simple, as F_{PV}^i changes are expected to have a minor impact on intrinsic state variable fluctuations and, even more, on DSSE uncertainty. In particular, F_{PV}^i is 1 most of time and it never becomes smaller than 0.94. In any case, the reactive power provided by the inverter is changed so as to keep the overall power factor associated to the net power injection at each bus equal to the value computed in nominal conditions.
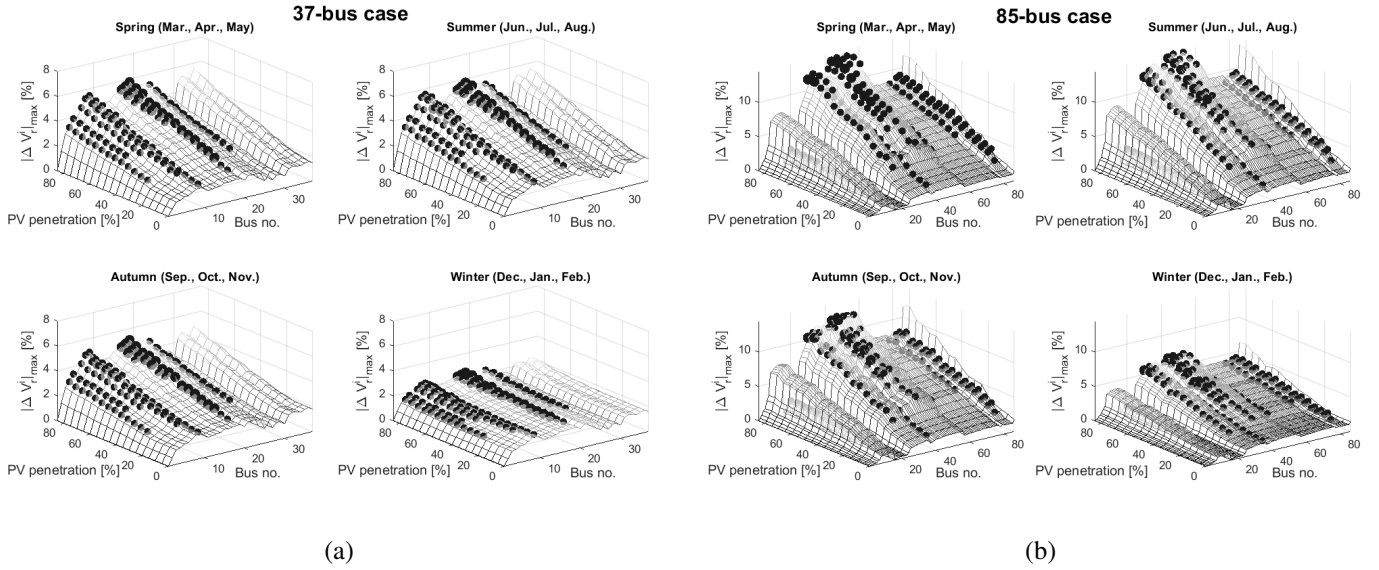
Figure 2: Absolute values of the maximum relative voltage variations at all buses of (a) the 37-bus case study and (b) the 85-bus rural distribution system for increasing levels of PV penetration and in different seasons. Such relative variations are computed with respect to the bus voltage magnitudes obtained from the power flow analysis in nominal conditions. The black spheric markers highlight the buses where the PV generation units are placed. The marker size is proportional to the amount of PV peak power.

The PV penetration level (namely the ratio between the total peak PV power available in the grid and the corresponding total maximum apparent load power) is increased gradually from 0% to 80% by steps of 5%. The buses to which PV units are linked are randomly chosen with uniform probability. However, the slack bus and the zero-injection buses are purposely excluded from PV unit placement. In this way, the size of subsystems 0 and 1 in (6) is not affected by PV penetration, thus ensuring a fair evaluation of the PV-IEKF estimation uncertainty in different conditions.

The algorithm adopted for PV unit deployment in both case studies is quite simple, as the purpose of this work is not to maximize the hosting capacity of the distribution systems considered, but rather to have a reasonable "ground truth" for state estimation even under stressed operating conditions due to the increasing PV penetration. In particular, once a new PV unit is linked to bus i and A_{PV}^i is computed accordingly (assuming nominal efficiency and temperature conditions), first F_{PV}^i is updated to maximize the active power injection at the same bus. Then, a static power flow analysis is performed to check whether, after a 5% PV penetration increment caused by the newly placed PV units, the RMS voltages at all buses lie within ±10% of the nominal values reported in Tab. 1 (for the 37-bus system) and in Tab. A.3.2 of [37] (for the 85-bus system). If this condition is met, then the PV units are retained and the algorithm starts over; otherwise, the PV units just placed at bus i are moved to a different one and bus i is permanently excluded from further installations of PV units. Of course, such a greedy approach does not return a unique deployment of PV units. However, it is sufficient to test the PV-IEKF state estimator under critical (although still reasonable) time-varying operating conditions, as it will be shown in Section 5.2 and 5.3.

4.2. Analysis of state variables intrinsic variations

Fig. 2(a)-(b) shows the absolute values of the maximum voltage variations at every bus of the 37-bus and the 85-bus distribution systems relative to the respective bus voltage magnitudes resulting from the power flow analysis in nominal conditions. Such maximum relative variations expressed in % are plotted for increasing levels of PV penetration and are grouped on a seasonal basis. The black spheric markers highlight the buses linked to one or more PV units. It is worth emphasizing that such variations are only due to the changeable load and PV generation conditions (with 15-minute resolution) over one year. Therefore, no measurement uncertainty, nor missing data affect the results of Fig. 2(a)-(b). This intermediate step is needed to compute the inherent state variable fluctuations that shall be estimated by the proposed PV-IEKF estimator. Indeed, as a rule of thumb, the DSSE uncertainty must be at least about one order of magnitude smaller than such inherent variations to provide trustworthy results, as it will be verified in Section 5.

The maximum absolute voltage phase variations at different buses (visually similar to those in Fig. 2 and not shown for the sake of brevity) never exceed ±2.5 centiradians (crad) in the 37-bus case and ±5 crad in the 85-bus case. Observe that the voltage changes tend to increase monotonically with PV penetration, as expected, although with significant differences between the two systems and from bus to bus. The voltage magnitude variations are well below ±10% (usually within ±5%) in the 37-bus case, while they may occasionally become greater than ±10% at some buses of the 85-bus distribution system (especially in late spring and summer), when the PV penetration level exceeds 60%. This result is reasonable if compared with the limits reported in the EN Standard 50160:2010 [3]. Moreover, the greedy algorithm used to place the PV units keeps into

account the *nominal* PV penetration level, whereas in practice the actual amounts of generated and consumed power at different times of the day may differ considerably from the respective peak values. Therefore, it may happen that the distribution systems operate under stressed conditions, especially in late spring and summer.

In conclusion, the fluctuations of the state variables in the test distribution systems considered are large enough, but not too critical, to run a trustworthy performance analysis of the PV-IEKF state estimator under different conditions of PV penetration.

5. DSSE performance evaluation

In this Section, the performance of the PV-IEKF estimator is analyzed in the case studies described in Section 4. In the following, first the state estimator settings as well as two possible measurement setups for DSSE implementation are described. Then, the state estimation results in the 37-bus and 85-bus case studies are reported and compared with those obtained with a classic WLS estimator in the very same experimental conditions. In the WLS case, the zero-injections are regarded as equality constraints of the optimization problem, which are eventually turned into auxiliary state variables. As a result, the solution is found through the so-called Lagrangian method [15].

5.1. State estimation settings and measurement setups

The settings of the PV-IEKF estimators in the prediction and update steps are reported below. It is worth emphasizing that, while the prediction step holds only for the PV-IEKF (no prediction exists with the WLS approach), the measurement setups that are adopted in the update step of the PV-IEKF are used for WLS estimation as well, in order to have a fair comparison.

5.1.1. Prediction step

The input sequences $\mathbf{d}_{G_k}^{m1}$ and $\mathbf{d}_{L_k}^{m1}$ for $m = \{\text{Jan.}, \ldots, \text{Dec.}\}$ used in (7) result from the backward Euler differences with 15-minute resolution of the daily average active and reactive PV generation and load profiles, respectively, computed over each month of the year. In particular, the sequence $\mathbf{d}_{G_k}^{m1}$ for a generic month m is computed as follows. First, the synthetic solar irradiance data used for power flow simulations in Section 4 are averaged at the same time of the day over all the days of month m prior to applying the first-order backward Euler difference. Then, the resulting differential average profiles are smoothed through a least-squares interpolation to make the mean values of error terms $\boldsymbol{\epsilon}_{G_k}^m$ approximately zero. Finally, the average differential solar irradiance profile is converted into active power by applying (14), and the reactive power is computed accordingly. In practice, the daily variations of active and reactive power in $\mathbf{d}_{G_k}^{m1}$ lie respectively within about ± 30 kW and ± 5 kvar in the 37-bus case and within about ± 20 kW and ± 3 kvar in the 85-bus case. Of course, such values depend on the time of the day, the season of the year and the PV penetration level.

The load differential variations $\mathbf{d}_{L_k}^{m1}$ at every bus are also estimated from the values referred to the same time of the day (i.e.

every 15 minutes) and averaged over every single month. The resulting active and reactive load variations in $\mathbf{d}_{L_k}^{m1}$ lie within about ± 7 kW and ± 4 kvar in the 37-bus case and within about ± 3 kW and ± 1 kvar in the 85-bus case, respectively, and they generally exhibit a smoother daily variability. The fluctuations $\boldsymbol{\epsilon}_{G_k}^m$ and $\boldsymbol{\epsilon}_{L_k}^m$ around $\mathbf{d}_{G_k}^{m1}$ and $\mathbf{d}_{L_k}^{m1}$, respectively, at different times of the day are eventually used to build covariance matrices $E_{G_k}^{m1}$ and $E_{L_k}^{m1}$ for $m = \{\text{Jan.}, \ldots, \text{Dec.}\}$ to be used in (8). In both case studies the standard deviations of the generated active and reactive power resulting from the block partition of $E_{G_k}^{m1}$ into active and reactive power components follow the same daily pattern of PV generation. The daytime maximum standard deviations of the active power variations over 15-minute intervals range from about 10-15 kW in winter to more than 60-80 kW in summer. The daytime maximum standard deviations of the respective reactive power variations range instead from about 1 kvar in winter to about 10 kvar in summer. The standard deviations of the load variations in $E_{L_k}^{m1}$ exhibit generally a much more uniform daily variability, although with some seasonal changes. In the 37-bus case, the maximum daily standard deviations of the active power load variations over 15-minute intervals range from about 5 kW to 10 kW with a few peaks exceeding 15 kW. The maximum daily standard deviations of the respective reactive power load variations range from about 2 kvar to 6 kvar. In the 85-bus case, the maximum daily standard deviations of the power load variations over 15-minute intervals are quite evenly spread between 4 kW and 7 kW (for active power) and between 3 kvar and 6 kvar (for reactive power). The elements of matrices Q_k^{00}, Q_k^{01}, Q_k^{10} and Q_k^{11} are in all cases between one or two orders of magnitude smaller than the elements of $G_{k-1}^{01}(E_{G_k}^{m1}+E_{L_k}^{m1})G_{k-1}^{01^T}$, $G_{k-1}^{01}(E_{G_k}^{m1} + E_{L_k}^{m1})G_{k-1}^{11^T}$ and $G_{k-1}^{11}(E_{G_k}^{m1}+E_{L_k}^{m1})G_{k-1}^{11^T}$ in (8) and (9), respectively. Therefore, the impact of process noise $\boldsymbol{\nu}_k$ on the predicted state covariance matrix is almost negligible.

5.1.2. Update step

As briefly introduced at the beginning of this Section, two measurement setups are assumed to be used to implement both the update step of the PV-IEKF and the WLS estimator. In the following, they will be shortly denoted as *Setup A* and *Setup B*, respectively, and the measurements included in the measurement vector $\mathbf{z}$ of (4) are summarized in Tab. 2. In *Setup A* only the active and reactive power injections P^i and Q^i at all buses along with the voltage magnitude V^1 at the slack bus are included in (4). With this set of measurements, local state observability is certainly preserved, since the observability matrix associated with the linearized system based on (2)-(4) has full rank. While the power measurements of subsystem 0 are all virtually zero, the power injections data at all buses of subsystem 1 result from the differences between the load and PV generation data collected by the remote terminal units of distribution SCADA systems. The PV units are assumed to be linked to power meters reporting measures every 15 minutes. As far as load monitoring is concerned, four possible scenarios of increasing technological complexity are considered. First, just the traditional pseudo-measurements, namely the mean values of the historical asynchronous load profiles collected from

Table 2: Measurement setups adopted for both the update step of the PV-IEKF and the WLS implementation. The list of measurements of either setup correspond to the those included in vector $\mathbf{z}$ of (4).

		Setup A	Setup B
Slack bus voltage		PQA*	PMU
P/Q Power inj.	PV Gen.	SMs at all generation sites linked up to 14 buses (37-bus case) or 17 buses (85-bus case)	SMs at all generation sites linked up to 14 buses (37-bus case) or 17 buses (85-bus case)
	Loads	Pseudo-measurements replaced by aggregated SM data (30%, 60% or 90%) from all buses	Pseudo-measurements replaced by aggregated SM data (30%, 60% or 90%) from all buses
	Zero-inj.	0 kW/kvar at 10 buses (37-bus case) or 20 buses (85-bus case)	0 kW/kvar at 10 buses (37-bus case) or 20 buses (85-bus case)
Bus voltage phasors		Not considered	From 1 to 13 PMUs (37-bus case) or from 1 to 17 buses (85-bus case) depending on the PV penetration level

*PQA = Power quality analyzer, PMU = Phasor Measurement Units, SM = Smart Meters.

legacy low-rate, low-accuracy meters are used. Then, 30%, 60% and finally 90% of such pseudo-measurements are replaced by the data collected at the same time of the day (i.e., every 15 minutes) from new-generation, high accuracy smart meters (SMs) [38]. Consider that the pseudo-measurement values can be also used to replace missing or bad data (e.g., due to communication problems), if they are detected before injecting the measurement data into any estimator.

Based on the assumptions above, the diagonal covariance matrices R_k^{00} and R_k^{11} in (12) are set as follows.

- The relative standard uncertainty of the slack bus voltage measured by a power quality analyzer is 0.31%, in line with the results reported in [48];

- The standard uncertainty of all zero-injection virtual power measurement is arbitrarily set to a very small dummy value (i.e. 10^{-6}) to avoid that R_k^{00} becomes singular.

- The standard uncertainties of the active and reactive power measurements of the loads linked to all buses of subsystem 1 result from the weighted sum of the standard uncertainties of pseudo-measurements and SM data. The weights depend on the share of SMs deployed (i.e., 0%, 30%, 60% and 90%). The uncertainty of pseudo-measurements is given by the monthly standard deviations of active and reactive loads with respect to the nominal load conditions at each bus. Such standard deviations typically range from about 10% to more than 30% of the respective nominal values. The measurement uncertainty of SM data results instead from the combination of various uncorrelated contributions computed as explained in [49], i.e. instrumental meter accuracy (±0.2%, ±0.5%, ±1%, or ±2% as reported in the IEC Standards 62053-21 and 62053-22), unexpected power losses along lines (up to ±1.5%), missing or bad data (up to ±4% of all SM data possibly replaced by pseudo-measurements), time synchronization errors (up to

few seconds, which may impact the results up to about ±1%) and voltage/current instrument transformers accuracy (between ±0.2% and ±1% depending on the transformer class) [50, 51]. As a result, the relative standard measurement uncertainty associated with SM data may range between 0.7% and 1.6% of readings, thus causing errors up to ±4.8% in the worst case.

Measurement *Setup B* relies not only on the same SCADA-based measurements of *Setup A*, but also on an increasing number of PMUs for distribution systems (e.g., the so-called micro-PMUs [52]), whose data are transferred to the so-called Phasor Data Concentrators through wired or wireless connections (e.g., the 4G mobile cellular network). Therefore, the phasor data related to crucial points of the distribution system complement (but do not replace) the traditional measurements at a reasonable cost and with no need for a major upgrade of the communication infrastructure. In addition, one PMU is assumed to replace the power quality analyzer at the slack bus, while the others are gradually deployed at all buses connected to one or more PV units. The PMUs are used to measure V^i and θ^i directly. As a result, the number of measurement equations in (10) as well as the size of R_k^{11} grows with the number of PMUs deployed in the grid. In compliance with the IEC/IEEE Standard 60255-118-1:2018 [53], the maximum Total Vector Error (TVE) of all PMUs has to be smaller than or equal to 1% in steady-state conditions. Assuming that i) voltage and phase measurement errors contribute evenly to the 99-th percentile of TVE values and ii) the amplitude and phase uncertainty contributions due to the limited accuracy of voltage transducers of Class 0.2 (reported for instance in [50]) are combined with the respective uncorrelated PMU instrumental uncertainty contributions, the total standard uncertainties of bus voltage amplitude and phase to be included in the main diagonal of R_k^{11} are set to 0.37% of the RMS voltage at time t_k and 0.44 crad, respectively.

5.2. State estimation uncertainty with measurement setup A

Fig. 3(a)-(b) shows the 99th percentiles of the relative amplitude (top) and phase (bottom) estimation errors as a function of the PV penetration level when measurement *Setup A* is considered. Such percentiles are computed over 1 simulated year at all buses of the 37-bus (a) and 85-bus (b) test distribution systems, after removing the initial PV-IEKF transient (about 1 day). Solid and dotted lines refer to the PV-IEKF and the WLS estimator, respectively. Different markers refer to increasing shares of aggregated SM data replacing traditional active and reactive power pseudo-measurements. Observe that the 99th percentiles of the relative amplitude estimation errors obtained with the PV-IEKF algorithm are much lower than both the relative maximum intrinsic fluctuations to be monitored [as desired, see Fig. 2(a)-(b)] and the values returned by the WLS estimator. Also, the PV-IEKF looks more sensitive to the use of smart metering technologies than the WLS estimator. Such results are consistent in both considered case studies. It is worth emphasizing that, while the bus voltage amplitudes exhibit intrinsic variations in the order of some percent (see Fig. 2), the 99th percentiles of the relative estimation errors obtained with the
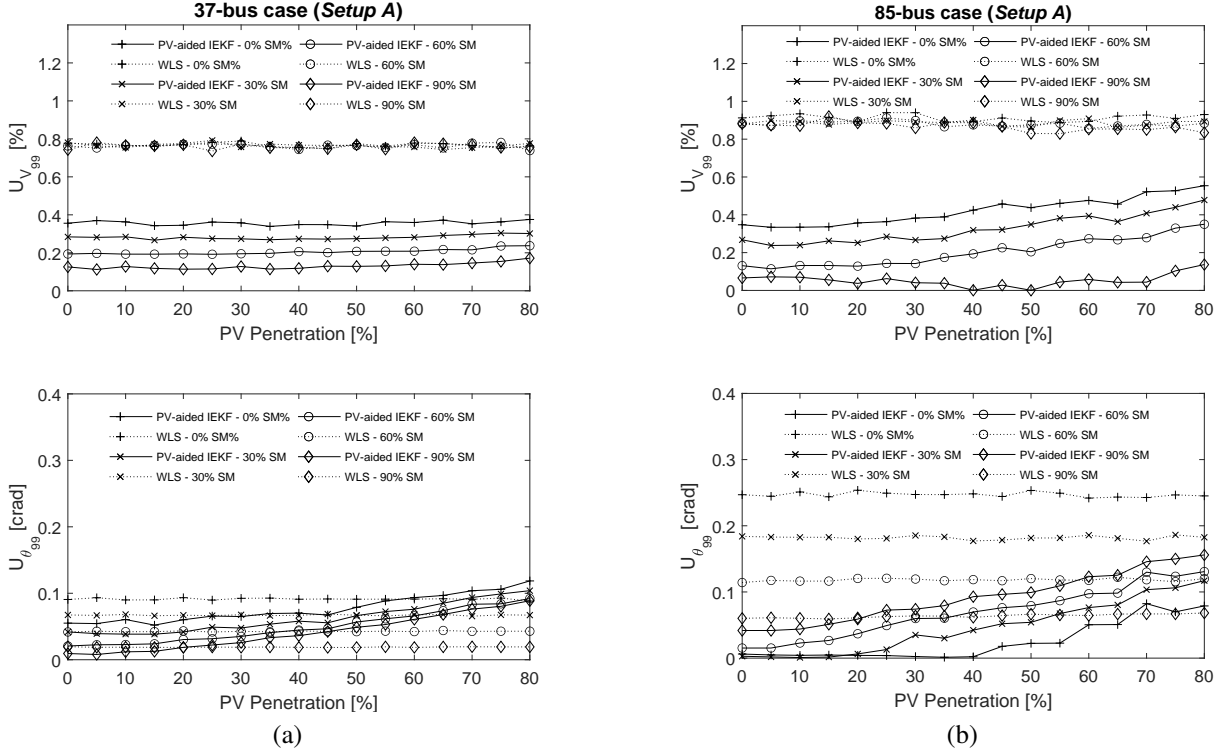
Figure 3: DSSE expanded uncertainties (with 99% confidence level) of relative amplitude (top) and phase (bottom) obtained with the PV-IEKF (solid lines) and WLS (dotted lines) state estimators as a function of the PV penetration level when the measurement *Setup A* (i.e., without PMUs) is considered. The 99th percentiles are computed from the relative deviations between the state variables estimated over one year at all buses of the 37-bus (a) and the 85-bus (b) distribution systems under test and the respective actual values obtained as explained in Section 4.2. In all graphs, different types of markers refer to increasing fractions of aggregated (and more accurate) SM data replacing pseudo-measurements.

PV-IEKF are steadily below 0.6% and can be so small as about 0.1%. Such values are from two to about ten times smaller than the WLS estimator ones. A deeper analysis (not shown for the sake of brevity) highlights that the DSSE error percentiles are quite similar at all buses, i.e. they are not particularly affected by distribution system topology.

As far as the estimation of phase state variables is concerned, the performance gap between the PV-IEKF and the WLS estimator is much smaller. In any case, again the 99th percentiles of phase estimation errors are more than one order of magnitude smaller than the maximum intrinsic phase variations due to load and PV generation only and mentioned in Section 4.2 (i.e., ±2.5 crad in the 37-bus case and ±5 crad in the 85-bus case). Therefore, both DSSE algorithms perform reasonably well. However, the performance gap between the PV-IEKF and the WLS estimator tends to increase with the size of the distribution system.

Further results, split by season and not shown for the sake of brevity, confirm that the 99th percentiles of the state estimation errors are quite independent of seasonal solar radiation changes.

One interesting issue that deserves attention is the apparently higher sensitivity of the PV-IEKF estimator to PV penetration than the WLS estimator. This phenomenon is probably due to the growing impact of the elements of $E_{G_k}^{m1}$ on the computation of the predicted state covariance matrix given by (8)-(9), and consequently, on the steady-state covariance of the estimated state. More in details, as the PV penetration increases, both

the number of nonzero elements of $E_{G_k}^{m1}$ and their magnitude (namely the variance of the PV power fluctuations around the average daily patterns in different months which are used as filter inputs in (7) obviously grow. However, such increments in prediction uncertainty are only partially counterbalanced by the use of the SM data collected from the PV units and used in the update step of the filter.

5.3. State estimation uncertainty with measurement setup B

Fig. 4(a)-(b) shows the DSSE expanded uncertainties (with 99% confidence) of relative amplitude (top) and phase (bottom) as a function of the PV penetration level when measurement *Setup B* is considered. Again, the 99th percentiles of the estimation errors are computed over 1 simulated year at all buses of the 37-bus (a) and 85-bus (b) distribution systems, after removing the initial PV-IEKF transient (about 1 day). Like in Fig. 3, solid and dotted lines refer to the PV-IEKF and the WLS estimator, respectively. Again, different markers refer to increasing shares of aggregated SM data that replace traditional active and reactive power pseudo-measurements. However, as explained in Section 5.1, in this case the PMUs are supposed to monitor the buses linked to PV units. Therefore, when the PV penetration increases, the number of deployed PMUs tends to grow as well. The results shown in Fig. 4(a)-(b) are globally consistent with those obtained with *Setup A*. The main difference in this case is that while the PMUs improve WLS state estimation considerably (especially amplitude state variables), their
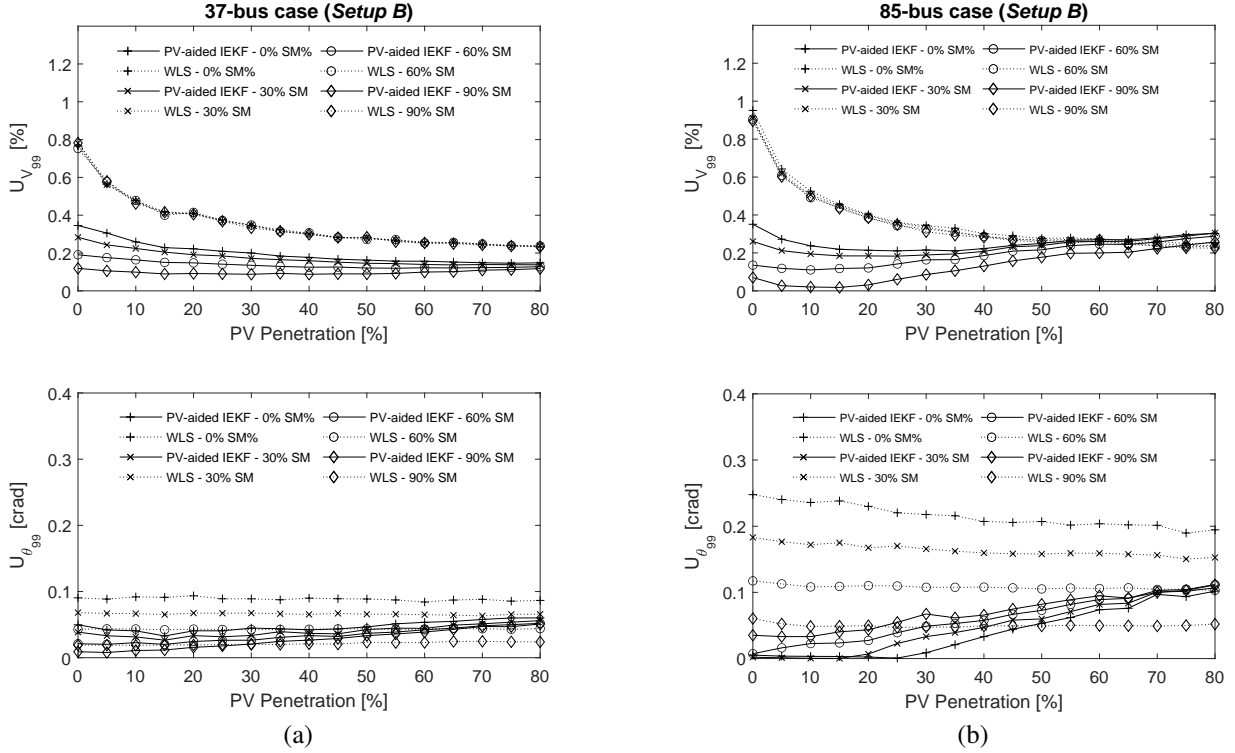
Figure 4: 99th percentiles of relative amplitude (top) and phase (bottom) estimation errors obtained with the PV-IEKF (solid lines) and WLS (dotted lines) algorithm as a function of the PV penetration level when the measurement *Setup B* (i.e., including PMUs) is considered. The 99th percentiles are computed from the relative deviations between the state variables estimated over one year at all buses of the 37-bus (a) and the 85-bus (b) distribution systems under test and the respective actual values obtained as explained in Section 4.2. In all graphs, different types of markers refer to increasing fractions of aggregated (and more accurate) SM data replacing pseudo-measurements.

impact on PV-IEKF results is minor. In fact, the performance of both estimators tend to converge when large PV penetration levels are achieved. Again, with the chosen input predictors, the WLS state estimator can be occasionally slightly more accurate than the PV-IEKF when the PV penetration exceeds 60%-70%. However, the PV-IEKF can provide excellent results (at least in quasi-steady state conditions) even if the grid is not strongly instrumented with PMUs, with significant potential savings for distribution systems operators.

5.4. Computational performance

The PV-IEKF and WLS algorithms were implemented in Matlab R2017b. The adopted processing platform is a workstation equipped with 128 GB of RAM, two Intel Xeon six-core E5 processors running at 2.2 GHz and Windows Server 2012 R2. The mean values and the standard deviations of the processing times needed to return a single state estimate of the 37-bus and the 85-bus distribution systems with either algorithm are shown in Tab. 3. The reported values result from the arithmetic average and the sampling standard deviations of 4000 estimates obtained by changing both the level of PV penetration and the measurement setup. In this respect, it was verified that the inclusion of PMUs in *Setup B* has a very small impact on the overall processing time (i.e. between 1% and 2% only). The results reported in Tab. 3 show that the processing times tends to grow almost quadratically with the number of buses. On the whole, the PV-IEKF estimator is more than 30% faster than the WLS

algorithm in either case study. This is due to the inherently iterative nature of the WLS approach that, even if generally requires less algebraic operations per step, takes several iterations to converge. Since the number of such iterations may change as a function of the system operating conditions, the processing time standard deviations of the WLS estimator are quite larger than those of the PV-IEKF.

Table 3: Mean values and standard deviations of the processing times needed to return a single state estimate of 37-bus and 85-bus test distribution systems.

	PV-IEKF		WLS	
	Mean	Std. dev.	Mean	Std. dev.
37-bus case	31 ms	4 ms	45 ms	8 ms
85-bus case	149 ms	6 ms	240 ms	34 ms

5.5. PV-IEKF convergence and response times

A typical issue affecting dynamic state estimators is the non-negligible number of steps needed to converge to the steady state. Such transients occur at the beginning (i.e., as a result of the chosen initial conditions) and after sudden changes of the state variables. Of course, no transient problems exist with the WLS estimator, because in that case in principle each estimate depends only on the measurement data collected at the same time and not on the previous states. In Tab. 4 the 99th percentiles of both the initial convergence times and the response

Table 4: 99th percentiles of the initial convergence times and of the response times to a sudden event (both expressed in normalized time steps) in the 37-bus and 85-bus cases for *Setup A* and *Setup B*, respectively.

	Setup A		*Setup B*	
	Initial transient	**Sudden event**	**Initial transient**	**Sudden event**
37-bus case	98	80	95	56
85-bus case	93	26	91	21

times to some sudden events in both test distribution systems are reported for *Setups A* and *B*, respectively. All values are expressed in discrete (i.e., normalized) time steps, to keep them independent of the sampling period. In the present study, the convergence and response times of a given state variable are defined as the time intervals between the first time step or the time step at which a sudden event occurs, respectively, and the time step after which the estimation errors of the same state variable lie within an interval centered in the steady-state value with 99% confidence. The step events were generated by applying three alternative sudden line impedance changes between buses 4–27, 14–34 and 11–28 in the 37-bus case and between buses 11–12, 67–68 and 32–33 in the 85-bus case. Such changes cause step-like variations (up to about 20%) of the state variables. The 99th percentiles of both the convergence times and the event response times are computed over all state variables by changing the PV penetration level and the shares of pseudo and SM data, as explained in the previous Sections. However, in Tab. 4 just the global percentiles of the aggregated data are shown for brevity, since we observed that the convergence and response times weakly depend on either the PV-based information or the share of SM data. The results in the Table show that the initial transients are quite consistent in all cases, whereas a remarkable difference exist between the two test distribution systems when a sudden event occurs. Such a difference makes sense because the relative impact of a given event on a large distribution system is expected to be lower than on a small one, as the buses that are farther from the event location are certainly less affected. Note that the use of PMUs generally tends to reduce the convergence and transient times. Of course, a much better responsiveness could be achieved if PMU data were injected into the PV-IEKF estimator at a higher rate (as typically ensured by this kind of instruments), provided that the bandwidth of the monitoring infrastructure is able to withstand massive streams of real-time data. Although the convergence performance of the PV-IEKF estimator looks globally reasonable, probably even better results in the case of step changes could be achieved by multiplying the covariance matrix of the predicted state by a *fudge factor* (namely a heuristic diagonal, positive definite matrix) just before computing the Kalman gain whenever the innovation term exceeds a given critical threshold [36].

5.6. Discussion on DSSE time resolution

As explained above, the results reported in this paper are obtained with a simulation time step of 15 minutes. Therefore,

they are too coarse to provide ultimate conclusions on high-rate state fluctuations. Nonetheless, the performance analysis clearly shows the accuracy improvement that can be achieved at a low cost by using just state-of-the-art monitoring technologies (most notably last-generation SMs) and the available input data on PV generation. Quite importantly, since the whole underlying theoretical formulation does not depend on the sampling period, the proposed PV-IEKF estimator can be potentially applied at higher rates, if the rate of input and measurement data is also larger. However, if very high state estimation rates are needed (i.e., in the order of 1 Hz or more), two main problems may arise. First, when the time step used for system discretization is comparable with the time constants of the grid, some equations of the model could become quite inaccurate, especially under transient conditions. Second, the distribution system should be fully observed by PMUs since, to the best of Authors' knowledge, no other instruments for grid monitoring can steadily collect and stream measurement data with reporting periods well below 1 s. Unfortunately, a widespread PMU deployment (although highly desirable from the technical point of view) could be infeasible for cost reasons or installation constraints. Moreover, the bandwidth of the whole communication infrastructure should able to withstand the data tsunami created by the PMUs themselves. Currently, in many countries this is not possible yet.

6. Conclusions

In this paper, a study about the potential benefits of the use of PV generation data for distribution system state estimation (DSSE) is reported. In particular, a PV-aided Interlaced Extended Kalman Filter (PV-IEKF) is proposed. The advantage of the PV-IEKF is twofold. First, the state estimation uncertainty is generally lower than the uncertainty achievable with a classic WLS algorithm, which is still the most common approach adopted at the distribution level. Second, compared to a standard Extended Kalman Filter implementation, the proposed interlaced solution makes the estimator inherently more robust, from the numerical point of view, to the ratio between the variance of power injections at buses where load and PV generation exhibit large fluctuations and the variance of virtual measurements at zero-injection buses. Finally, the PV-IEKF is computationally faster than the WLS algorithm and, in quasi-steady-state operating condition, it generally provides very accurate results even when a small number of Phasor Measurement Units (PMUs) is used.

The results obtained in this paper suggest that even better results could be achieved if more accurate solar generation forecasting algorithms are used to support state estimation. This might also reduce the present sensitivity to PV penetration that, although not particularly critical, is probably due to the chosen input model. The analysis presented in the paper is performed at low reporting rates, i.e., considering the communication constraints of most of the existing infrastructures for distribution systems monitoring. However, the PV-IEKF could be implemented to return state estimates at quite higher rates (e.g., ev-

ery second) by combining short-term PV forecasting models and widespread PMU data.

Finally, it is worth emphasizing that the proposed approach could be potentially extended or adapted to other forms of renewable-based distributed generators, provided that i) the average daily power generation profiles and their variances can be reconstructed with a good time resolution (to feed the prediction step of the filter) and ii) the power generation data can be telemetered in real-time (for state estimation update).

Appendix A – Discretized system model

Given the definitions of $\mathbf{x}$, $\mathbf{u}_L$ and $\mathbf{u}_G$ introduced in Section 3, the power injections expressions in (1) for $i = 2, \ldots, N$ can be rearranged in an implicit matrix form as

$$\begin{bmatrix} \mathbf{f}_P(\mathbf{x}, \mathbf{u}_G, \mathbf{u}_L) \\ \mathbf{f}_Q(\mathbf{x}, \mathbf{u}_G, \mathbf{u}_L) \end{bmatrix} = \mathbf{0}. \tag{A.1}$$

Observe that, if input vectors $\mathbf{u}_G$ and $\mathbf{u}_L$ are given, (A.1) is a nonlinear system of $2N - 2$ equations in $2N - 1$ unknowns. Therefore, the system is underdetermined. The active and reactive power injections at the slack bus are purposely not included in (A.1), because P^1 and Q^1 generally depend linearly on the power injections at all the other buses. However, since the RMS voltage amplitude at the slack bus is supposed to be equal to a given nominal value $\bar{V}$, the undertermined system (A.1) can be turned into a balanced one (i.e. with $2N - 1$ equations in $2N - 1$ unknowns) by adding equation $V^1 - \bar{V} = 0$, i.e.

$$\mathbf{f}(\mathbf{x}, \mathbf{u}_G, \mathbf{u}_L) = \begin{bmatrix} V^1 - \bar{V} \\ \mathbf{f}_P(\mathbf{x}, \mathbf{u}_G, \mathbf{u}_L) \\ \mathbf{f}_Q(\mathbf{x}, \mathbf{u}_G, \mathbf{u}_L) \end{bmatrix} = \mathbf{0}. \tag{A.2}$$

Recalling that both state variables and input active/reactive power injections are time-varying quantities, the evolution of system (A.1) between instants t_{k-1} and t_k (assuming that the difference $t_k - t_{k-1}$ is small enough compared with the system time constants) can be approximately described by the first-order Taylor's series expansion of (A.1) [24], i.e.

$$A_{k-1}\Delta\mathbf{x}_k + B_{k-1}(\Delta\mathbf{u}_{G_k} - \Delta\mathbf{u}_{L_k}) + \mathbf{e}_k = \mathbf{0}, \tag{A.3}$$

where $\Delta\mathbf{x}_k = \mathbf{x}_k - \mathbf{x}_{k-1}$, $\Delta\mathbf{u}_{G_k} = \mathbf{u}_{G_k} - \mathbf{u}_{G_{k-1}}$ and $\Delta\mathbf{u}_{L_k} = \mathbf{u}_{L_k} - \mathbf{u}_{L_{k-1}}$ are the state, load and power generation variations in one time step, $\mathbf{e}_k$ is the linearization error,

$$A_{k-1} = \frac{\partial\mathbf{f}}{\partial\mathbf{x}}\bigg|_{\substack{\mathbf{x}=\mathbf{x}_{k-1}\\ \mathbf{u}_G=\mathbf{u}_{G_{k-1}}\\ \mathbf{u}_L=\mathbf{u}_{L_{k-1}}}} = \begin{bmatrix} 0 & \cdots & 0 & 1 & \cdots & 0 \\ \frac{\partial\mathbf{f}_P}{\partial\theta^2} & \cdots & \frac{\partial\mathbf{f}_P}{\partial\theta^N} & \frac{\partial\mathbf{f}_P}{\partial V^1} & \cdots & \frac{\partial\mathbf{f}_P}{\partial V^N} \\ \frac{\partial\mathbf{f}_Q}{\partial\theta^2} & \cdots & \frac{\partial\mathbf{f}_Q}{\partial\theta^N} & \frac{\partial\mathbf{f}_Q}{\partial V^1} & \cdots & \frac{\partial\mathbf{f}_Q}{\partial V^N} \end{bmatrix} \tag{A.4}$$

is the $(2N-1)\times(2N-1)$ Jacobian of $\mathbf{f}(\mathbf{x}, \mathbf{u}_G, \mathbf{u}_L)$ with respect to the state vector variables at time t_{k-1}, and finally

$$B_{k-1} = \frac{\partial\mathbf{f}}{\partial\mathbf{u}_L}\bigg|_{\substack{\mathbf{x}=\mathbf{x}_{k-1}\\ \mathbf{u}_G=\mathbf{u}_{G_{k-1}}\\ \mathbf{u}_L=\mathbf{u}_{L_{k-1}}}} = \begin{bmatrix} \mathbf{0}^T & \mathbf{0}^T \\ I_{N-1} & 0_{N-1} \\ 0_{N-1} & I_{N-1} \end{bmatrix} \tag{A.5}$$

is the Jacobian of $\mathbf{f}(\mathbf{x}, \mathbf{u}_G, \mathbf{u}_L)$ with respect to the input variables, with I_{N-1} and 0_{N-1} being the $(N-1)\times(N-1)$ identity and zero matrices, respectively. Observe that while A_{k-1} changes with time, B_{k-1} is constant. If A_{k-1} is a full-rank matrix, i.e. invertible (this assumption is generally true since load and PV generation at buses different from the slack bus are not linearly dependent), then equation (A.3) can be rewritten as

$$\mathbf{x}_k = \mathbf{x}_{k-1} - A_{k-1}^{-1}B_{k-1}(\Delta\mathbf{u}_{G_k} - \Delta\mathbf{u}_{L_k}) - A_{k-1}^{-1}\mathbf{e}_k, \tag{A.6}$$

from which (2) finally results.

Appendix B – Benefits of Blockwise Inverse Computation in PV-IEKF Implementation

If the so-called blockwise inversion lemma is applied to (12), the inverse of the overall innovation covariance matrix $S_k = \begin{bmatrix} S_k^{00} & S_k^{01} \\ S_k^{01^T} & S_k^{11} \end{bmatrix}$ can be split into the following blocks, i.e.

$$\begin{aligned} L_k^{00} &= (S_k^{00} - S_k^{01}S_k^{11^{-1}}S_k^{01^T})^{-1} \\ L_k^{01} &= -(S_k^{00} - S_k^{01}S_k^{11^{-1}}S_k^{01^T})^{-1}S_k^{01}S_k^{11^{-1}} \\ L_k^{10} &= L_k^{01^T} = S_k^{11^{-1}}S_k^{01^T}(S_k^{00} - S_k^{01}S_k^{11^{-1}}S_k^{01^T})^{-1} \\ L_k^{11} &= S_k^{11^{-1}} + S_k^{11^{-1}}S_k^{01^T}(S_k^{00} - S_k^{01}S_k^{11^{-1}}S_k^{01^T})^{-1} \end{aligned} \tag{B.1}$$

Observe that, in (B.1) the inverse of both S_k^{11} and its Schur's complement $\tilde{S}_k^{11} = S_k^{00} - S_k^{01}S_k^{11^{-1}}S_k^{10}$ have to be computed. Therefore, it is essential that i) both S_k^{11} and $\tilde{S}_k^{11}$ are not singular; ii) their condition number is small enough to avoid ill-conditioning problems. The first property results from the fact that a block diagonal matrix is positive definite if and only if each diagonal block is positive definite. Therefore, both S_k^{00} and S_k^{11} must be positive definite. Moreover, $\tilde{S}_k^{11}$ results from the difference of two positive definite matrices. Thus, it must also be positive definite.

As far as the second property is concerned, the cases of S_k^{11} and $\tilde{S}_k^{11}$ have to be analyzed independently. As to S_k^{11}, let $s_{min} = s_1 \leq \cdots \leq s_N = s_{max}$ be the eigenvalues of S_k and N_0 be the number of zero injection buses. The principal submatrices S_k^l of S_k (for $l = 1, \ldots, N_0$) obtained by removing recursively, one at a time, the rows and the columns of S_k associated with zero-power injections are of course positive definite. Let us refer to $0 < s_1^l \leq s_2^l \leq \cdots \leq s_{N-r}^l$ as the eigenvalues of matrix S_k^l of size $N - l$. Due to the *Cauchy's interlacing inequality*, the jth eigenvalue s_j^l of any principal submatrix S_k^{l+1} of S_k^l of size $N - l - 1$ lies in the interval $s_j^l \leq s_j^{l+1} \leq s_{j+1}^l$ for $j = 1, \ldots, N-l-1$. As a consequence, $s_{min}^l \leq s_{min}^{l+1}$, $s_{max}^{l+1} \leq s_{max}^l$ and, more in general,

$$s_{min} \leq s_{min}^1 \ldots \leq s_{min}^{N_0} \quad \text{and} \quad s_{max}^{N_0} \leq s_{min}^{N_0-1} \ldots \leq s_{max}. \tag{B.2}$$

Therefore, the condition number of S_k^{11} cannot be greater (and most likely it will be strictly smaller) than the condition number of the whole innovation covariance matrix, i.e. $r(S_k^{11}) = \frac{s_{max}^{N_0}}{s_{min}^{N_0}} \leq \frac{s_{max}}{s_{min}}$.

Observe that S_k can be rearranged as

$$S_k = M_k + \Gamma_k = \begin{bmatrix} \tilde{S}_k^{11} & 0 \\ 0 & 0 \end{bmatrix} + \begin{bmatrix} S_k^{01} S_k^{11^{-1}} S_k^{01^T} & S_k^{01} \\ S_k^{01^T} & S_k^{11} \end{bmatrix}. \quad \text{(B.3)}$$

Let $\mu_1 \leq \cdots \leq \mu_N$ and $\gamma_1 \leq \cdots \leq \gamma_N$ be the eigenvalues of matrices M_k and Γ_k, respectively. Since Γ_k is positive semidefinite with a null space of size N_0, by applying the Courant-Fischer minimax principle, it follows that $s_{min} \leq \mu_k$. Of course, the minimum nonzero eigenvalues of M_k and $\tilde{S}_k^{11}$ coincide, i.e. $\tilde{s}_{min} = \mu_k$. On the other hand, it is known from the Weyl theorem (which provides the upper and lower bounds to the eigenvalues of the sum of two Hermitian matrices) that $s_{max} \geq \mu_N + \gamma_1$. Thus, recalling that the maximum eigenvalue of $\tilde{S}_k^{11}$ is $\tilde{s}_{max} = \mu_N$ and $\gamma_1 = 0$ (as Γ_k is positive semidefinite), it finally results that the condition number of $\tilde{S}_k^{11}$ cannot be greater than the condition number of the whole innovation covariance matrix, i.e. $r(\tilde{S}_k^{11}) = \frac{\tilde{s}_{max}}{\tilde{s}_{min}} = \frac{\mu_N}{\mu_k} \leq \frac{s_{max}}{s_{min}}$.

In conclusion, the condition numbers of S_k^{11} and $\tilde{S}_k^{11}$ obtained from the blockwise inversion of S_k (which in turn is partitioned by the interlaced EKF implementation described in Section 3.2) are lower than (or equal to, but it is very unlikely) the condition number of the overall EKF innovation covariance matrix.

References

[1] EPIA, Global market outlook for solar power 2018-2022 (2018) 1–81. URL http://www.solarpowereurope.org/global-market-outlook-2018-2022/

[2] Electric power systems and equipment - voltage ratings (60 hertz), ANSI C84.1-2016 (2016) 1–21.

[3] Voltage characteristics of electricity supplied by public electricity networks, EN 50160:2010 (Dec. 2010).

[4] M. Karimi, H. Mokhlis, K. Naidu, S. Uddin, A. Bakar, Photovoltaic penetration issues and impacts in distribution network a review, Renewable and Sust. Energy Reviews 53 (2016) 594 – 605.

[5] K. Turitsyn, P. Sulc, S. Backhaus, M. Chertkov, Options for control of reactive power by distributed photovoltaic generators, Proc. IEEE 99 (6) (2011) 1063–1073.

[6] F. Ding, B. Mather, On distributed PV hosting capacity estimation, sensitivity study, and improvement, IEEE Trans. Sustain. Energy 8 (3) (2017) 1010–1020.

[7] F. Ahmad, A. Rasool, E. Ozsoy, R. Sekar, A. Sabanovic, M. Elitas, Distribution system state estimation-a step towards smart grid, Renewable and Sustainable Energy Reviews 81 - part 2 (2018) 2659 – 2671.

[8] D. Della Giustina, M. Pau, P. Pegoraro, F. Ponci, S. Sulis, Electrical distribution system state estimation: measurement issues and challenges, IEEE Instrumentation Measurement Magazine 17 (6) (2014) 36–42.

[9] I. Cobelo, A. Shafiu, N. Jenkins, G. Strbac, State estimation of networks with distributed generation, European Transactions on Electrical Power 17 (1) (2007) 21–36.

[10] D. Macii, G. Barchi, D. Moser, Impact of PMUs on state estimation accuracy in active distribution grids with large PV penetration, in: Proc. of IEEE Workshop on Environmental, Energy, and Structural Monitoring Systems (EESMS), Trento, Italy, 2015, pp. 72–77.

[11] M. Ayiad, H. Martins, O. Nduka, B. Pal, State Estimation of Low Voltage Distribution Network With Integrated Customer-Owned PV and Storage Unit, in: Proc. IEEE PowerTech, Milan, Italy, 2019, pp. 1–6.

[12] L. Schenato, G. Barchi, D. Macii, R. Arghandeh, K. Poolla, A. V. Meier, Bayesian linear state estimation using smart meters and pmus measurements in distribution grids, in: Proc. of IEEE International Conference on Smart Grid Communications (SmartGridComm), Venice, Italy, 2014, pp. 572 – 577.

[13] S. Chakrabarti, E. Kyriakides, M. Albu, Uncertainty in power system state variables obtained through synchronized measurements, IEEE Trans. on Instr. Meas. 58 (8) (2009) 2452–2458.

[14] A. Primadianto, C. Lu, A review on distribution system state estimation, IEEE Trans. Power. Syst. 32 (5) (2017) 3875–3883.

[15] A. Abur, A. Exposito, Power System State Estimation (Theory and Implementation), Marcel Dekker, 2004.

[16] V. Kirinčić, J. Lerga, N. Saulig, D. Franković, Improved power system state estimator with preprocessing based on the modified intersection of confidence intervals, Sustainable Energy, Grids and Networks 21 (2020) 100323.

[17] T. Chen, Robust state estimation for power systems via moving horizon strategy, Sustainable Energy, Grids and Networks 10 (2017) 46 – 54.

[18] A. M. Kettner, M. Paolone, Sequential discrete Kalman filter for real-time state estimation in power distribution systems: Theory and implementation, IEEE Trans. on Instr. Meas. 66 (9) (2017) 2358–2370.

[19] A. M. L. da Silva, M. B. D. C. Filho, J. F. de Queiroz, State forecasting in electric power systems, IEE Proceedings C - Generation, Transmission and Distribution 130 (5) (1983) 237–244.

[20] J. Zhao, M. Netto, L. Mili, A robust iterated extended Kalman filter for power system dynamic state estimation, IEEE Transactions on Power Systems 32 (4) (2017) 3205–3216.

[21] J. Qi, K. Sun, J. Wang, H. Liu, Dynamic state estimation for multi-machine power system by Unscented Kalman Filter with enhanced numerical stability, IEEE Transactions on Smart Grid 9 (2) (2018) 1184–1196.

[22] P. Rousseaux, D. Mallieu, T. Van Cutsem, M. Ribbens-Pavella, Dynamic state prediction and hierarchical filtering for power system state estimation, Automatica 24 (5) (1988) 595 – 618.

[23] J. Zhao, A. Gómez-Expósito, M. Netto, L. Mili, A. Abur, V. Terzija, I. Kamwa, B. Pal, A. K. Singh, J. Qi, Z. Huang, A. P. S. Meliopoulos, Power system dynamic state estimation: Motivations, definitions, methodologies, and future work, IEEE Transactions on Power Systems 34 (4) (2019) 3188–3198.

[24] S. Sarri, M. Paolone, R. Cherkaoui, A. Borghetti, F. Napolitano, C. Nucci, State estimation of active distribution networks: Comparison between WLS and iterated Kalman-filter algorithm integrating PMUs, in: Proc. IEEE PES Int. Conf. and Exhib. on Innovative Smart Grid Technologies (ISGT Europe), Berlin, Germany, 2012, pp. 1–8.

[25] Y. Huang, S. Werner, J. Huang, N. Kashyap, V. Gupta, State estimation in electric power grids: meeting new challenges presented by the requirements of the future grid, IEEE Signal Processing Magazine 29 (5) (2012) 33–43.

[26] C. Muscas, M. Pau, P. A. Pegoraro, S. Sulis, Effects of measurements and pseudo-measurements correlation in distribution system state estimation, IEEE Trans. on Instr. Meas. 63 (12) (2014) 2813–2823. doi:10.1109/TIM.2014.2318391.

[27] C. Landi, G. Del Prete, D. Gallo, M. Luiso, The use of real-time instruments for smart power systems, in: Proc. IEEE Int. Energy Conf. and Exhib. (ENERGYCON), Florence, Italy, 2012, pp. 884–889.

[28] R. Khorshidi, F. Shabaninia, T. Niknam, A new smart approach for state estimation of distribution grids considering renewable energy sources, Energy 94 (2016) 29 – 37.

[29] T. Niknam, B. B. Firouzi, A practical algorithm for distribution state estimation including renewable energy sources, Renewable Energy 34 (11) (2009) 2309 – 2316.

[30] J. Liu, J. Tang, F. Ponci, A. Monti, C. Muscas, P. Pegoraro, Trade-offs in PMU deployment for state estimation in active distribution grids, IEEE Transactions on Smart Grid 3 (2) (2012) 915–924.

[31] T. Chen, A PMU-based state estimator considering classic HVDC links under different control modes, Sustainable Energy, Grids and Networks 2 (2015) 69 – 82.

[32] M. Pau, P. Pegoraro, S. Sulis, Efficient branch-current-based distribution system state estimation including synchronized measurements, IEEE Trans. on Instr. Meas. 62 (9) (2013) 2419–2429.

[33] D. Macii, Z. Aziz, D. Fontanelli, Uncertainty analysis of distribution system state estimation based on Extended Kalman Filtering and phasor measurement units, in: Proc. IEEE Int. Instr. and Meas. Tech. Conf. (I2MTC), Auckland, New Zealand, 2019, pp. 1–6.

[34] Y. Guo, W. Wu, B. Zhang, H. Sun, An efficient state estimation algorithm considering zero injection constraints, IEEE Trans. Power. Syst. 28 (3)

(2013) 2651–2659.

[35] L. Glielmo, R. Setola, F. Vasca, An interlaced extended Kalman filter, IEEE Trans. Autom. Control 44 (8) (1999) 1546–1549.

[36] Y. Bar-Shalom, X. Rong Li, T. Kirubarajan, Estimation with Application to Tracking and Navigation – Theory, Algorithm and Software, John Wiley and Sons, 2001.

[37] D. Das, D. Kothari, A. Kalam, Simple and efficient method for load flow solution of radial distribution networks, International Journal of Electrical Power & Energy Systems 17 (5) (1995) 335 – 346.

[38] A. Pití, G. Verticale, C. Rottondi, A. Capone, L. Lo Schiavo, The role of smart meters in enabling real-time energy services for households: the Italian case, Energies 10 (2) (2017).

[39] R. D. Zimmerman, C. E. Murillo-Sanchez, R. J. Thomas, MATPOWER: Steady-state operations, planning, and analysis tools for power systems research and education, IEEE Trans. Power. Syst. 26 (1) (2011) 12–19.

[40] C. Sandels, D. Brodén, J. Widén, L. Nordström, E. Andersson, Modeling office building consumer load with a combined physical and behavioral approach: Simulation and validation, Applied Energy 162 (2016) 472 – 485.

[41] D. A. Brodén, K. Paridari, L. Nordström, Matlab applications to generate synthetic electricity load profiles of office buildings and detached houses, in: Proc. IEEE Innovative Smart Grid Technologies - Asia (ISGT-Asia), Auckland, New Zealand, 2017, pp. 1–6.

[42] G. Valverde, A. T. Saric, V. Terzija, Probabilistic load flow with non-gaussian correlated random variables using gaussian mixture models, IET Generation, Transmission Distribution 6 (7) (2012) 701–709.

[43] D. Q. Hung, N. Mithulananthan, K. Y. Lee, Determining PV penetration for distribution systems with time-varying load models, IEEE Trans. Power. Syst. 29 (6) (2014) 3048–3057.

[44] M. A. Green, Y. Hishikawa, E. D. Dunlop, D. H. Levi, J. HohlEbinger, M. Yoshita, A. W. HoBaillie, Solar cell efficiency tables (version 53), Progress in Photovoltaics 27 (1) (2019) 3–12.

[45] V. K. Sood, H. Abdelgawad, Chapter 14 - power converter solutions and controls for green energy, in: R. K. Chauhan, K. Chauhan (Eds.), Distributed Energy Resources in Microgrids, Academic Press, 2019, pp. 357 – 387.

[46] E. Dall'Anese, S. V. Dhople, G. B. Giannakis, Optimal dispatch of photovoltaic inverters in residential distribution systems, IEEE Trans. Sustain. Energy 5 (2) (2014) 487–497.

[47] S. Ghosh, S. Rahman, M. Pipattanasomporn, Distribution voltage regulation through active power curtailment with PV inverters and solar generation forecasts, IEEE Trans. Sustain. Energy 8 (1) (2017) 13–22.

[48] A. Cataliotti, V. Cosentino, S. Guaiana, S. Nuccio, D. D. Cara, N. Panzavecchia, G. Tinè, Measurement uncertainty impact on simplified load flow analysis in MV smart grids, in: Proc. IEEE Int. Instr. and Meas. Tech. Conf. (I2MTC), Houston, TX, USA, 2018, pp. 1–6.

[49] F. Ni, P. H. Nguyen, J. F. G. Cobben, H. E. van den Brom, D. Zhao, Uncertainty analysis of aggregated smart meter data for state estimation, in: Proc. IEEE Int. Workshop on Applied Measurements for Power Systems (AMPS), Aachen, Germany, 2016, pp. 1–6.

[50] H. Carstens, X. Xia, S. Yadavalli, Measurement uncertainty in energy monitoring: Present state of the art, Renewable and Sustainable Energy Reviews 82 (2018) 2791 – 2805.

[51] M. Asprou, E. Kyriakides, M. Albu, The effect of variable weights in a WLS state estimator considering instrument transformer uncertainties, IEEE Trans. on Instr. Meas. 63 (6) (2014) 1484–1495.

[52] A. von Meier, D. Culler, A. McEachern, R. Arghandeh, Micro-synchrophasors for distribution systems, in: IEEE PES Innovative Smart Grid Technologies Conference (ISGT), Washington, DC, USA, 2014, pp. 1–5.

[53] IEEE/IEC International Standard - Measuring relays and protection equipment - Part 118-1: Synchrophasor for power systems - Measurements, IEC/IEEE 60255-118-1:2018 (2018) 1–78.